Journal of Power Sources 192 (2009) 400–407

Contents lists available at ScienceDirect

Journal of Power Sources

journal homepage: www.elsevier.com/locate/jpowsour

Thermal stress modeling of anode supported micro-tubular solid oxide fuel cell

Daan Cui [a,b,c], Mojie Cheng [a,b,*]

[a] Dalian National Laboratory for Clean Energy, Dalian 116023, PR China
[b] Dalian Institute of Chemical Physics, Chinese Academy of Sciences, 457 Zhongshan Road, Dalian, Liaoning 116023, PR China
[c] Graduate School of the Chinese Academy of Sciences, Beijing 100049, PR China

ARTICLE INFO

Article history:
Received 18 December 2008
Received in revised form 25 March 2009
Accepted 25 March 2009
Available online 2 April 2009

Keywords:
Solid oxide fuel cell
Micro-tube
Modeling
Thermal stress

ABSTRACT

An anode-supported micro-tubular solid oxide fuel cell (SOFC) is analyzed by a two-dimensional axisymmetric numerical model, which is validated with the experimental *I–V* data. The temperature distribution generated by the thermo-electrochemical model is used to calculate the thermal stress field in the tubular SOFC. The results indicate that the current transport in the anode is the same at every investigated position. The stress of the micro-tubular cell occurs mainly because of the residual stress due to the mismatch between the coefficients of thermal expansion of the materials of the membrane electrode assembly. The micro-tubular cell can operate safely, but if there is an interfacial defect or a high enough tensile stress applied at the electrolyte, a failure can arise.

1. Introduction

The solid oxide fuel cell (SOFC) is one of the most promising candidates for power generation because of their high efficiency, clean generation of electric power and silent work [1,2]. Currently, the SOFC prototypes have proven its ability to achieve high electrical efficiency, especially for a hybrid system with gas turbine. Several different cell designs are being investigated [1–6]. Compared with the planar SOFC, the tubular one has several advantages as mentioned in literature [2,4–6]. Recently, because of a faster start-up and higher volume power density, the anode-supported micro-tubular SOFC has been rapidly developed [2,4,5]. The present main concerns to SOFC commercialization are the high manufacturing costs and short lifetime. The structural failure is one of major issues for the high degradation rates.

Many investigations have been carried out on the thermo-electrochemical modeling of the tubular and planar SOFC [2–4,7–9], however, only a few have been carried on thermal stress up. Two types of thermal stress are present in a SOFC. The first one is the residual stress due to the mismatch between the coefficients of thermal expansion (CTE) of the materials of the membrane electrode assembly (MEA). Finite element method has been employed to simulate the cell stress [3,6,9,10]. The second one is thermal mismatch stress due to temperature gradient at operating conditions. Selimovic et al. [3] and Nakajo et al. [6] have coupled their thermo-electrochemical model with a finite-element tool to simulate the stress in the cell during operation. In order to quantify and predict the magnitude of the thermal stress in a micro-tubular SOFC, a more specific model should be developed.

In this study, a two-dimensional (2D) axisymmetric numerical model is set up to analyze an anode-supported micro-tubular SOFC. The model presented in this paper covers momentum, electrochemical, heat-species transport and the thermal stress analysis. The simulation of the *I–V* characteristics versus the experimental data from the cell performance tests is carried out. The main purpose of the present work is to study the characteristics of the stress field including the residual stress and thermal mismatch stress. The approach is to couple a thermo-electrochemical model for the computation of the temperature field. After that, the temperature field is imported to the structural mechanics module and the stress field is solved. Temperature gradients and thermal stress between the components are evaluated. The Weibull approach is developed to investigate the effects of the stress on the MEA reliability.

2. Experimental

2.1. Fabrication of anode-supported micro-tubular SOFC

A green NiO/YSZ tubular support is prepared by an extrusion method. An equal weight of commercial nickel oxide (NiO, J. T. Baker Corporation) and 8 mol% yttria stabilized zirconia (YSZ, Tosoh Corporation) are used. After the extruded tube is dried, a thin film of the YSZ electrolyte is coated on the tube. The electrolyte–anode bilayered tube is then co-fired at 1723 K for 4 h. A $La_{0.80}Sr_{0.20}MnO_3$

* Corresponding author at: Dalian Institute of Chemical Physics, Chinese Academy of Sciences, 457 Zhongshan Road, Dalian, Liaoning 116023, PR China.
Tel.: +86 411 84379049; fax: +86 411 84379049.
E-mail address: mjcheng@dicp.ac.cn (M. Cheng).

0378-7753/$ – see front matter © 2009 Elsevier B.V. All rights reserved.
doi:10.1016/j.jpowsour.2009.03.046

Nomenclature

c	concentration [mol m^{-3}]
C_P	specific heat capacity [J mol^{-1} K^{-1}]
D_{ij}	diffusion coefficient [m^2 s^{-1}]
E	Young's modulus [GPa]
F	Faraday's constant [96485 C mol^{-1}]
i	local current density [A m^{-2}]
i_0	exchange current density [A m^{-2}]
k	thermal conductivity [W m^{-1} K^{-1}]
K	permeability [m^2]
m	Weibull modulus
n_e	electron transferred per reacting
P	pressure [Pa]
P_f	failure probability
q	heat source [W m^{-2}]
Q	volumetric heating rate [W m^{-3}]
R_g	gas constant [8.314 J mol^{-1} K^{-1}]
T	temperature [K]
T_{ref}	reference temperature [K]
u	velocity [m s^{-1}]
V_0	reference volume [mm^3]

Greek letters

α	thermal expansion coefficient [K^{-1}]
β	transfer coefficient
ε_{rad}	thermal radiative emissivity
ε_t	the total strain
ε_{th}	thermal strain
η	overpotential [V]
μ	dynamic viscosity [m^2 s^{-1}]
ρ	density [kg m^{-3}]
σ	conductivity [S m^{-1}]
σ_0	Stefan–Boltzmann constant [5.67 × 10^{-8} W m^2 K^4]
$\sigma_{s,0}$	characteristic strength [MPa]
σ_s	stress [MPa]
ν	Poisson's ratio
ϕ	potential [V]

Subscripts and superscripts

a	anode
act	activation
c	cathode
ele	electrolyte
j	cell component (anode, electrolyte and cathode)
rad	radiation
rev	reversible
t	total
0	standard

(LSM)/YSZ composite cathode is slurry-coated on the YSZ film, and then fired at 1523 K for 2 h. The dimensions of the cell are listed in Table 1.

2.2. Single cells measurements

Fig. 1 shows the diagram of the micro-tubular cell reactor. The tubular cell is located at the center of a furnace with a furnace wall temperature of 1073 K. The inlet fuel is composed of H_2 and H_2O (0.97:0.03 in molar fractions), flowing at a volume flow rate of 20 cm^3 min^{-1} at room temperature. The fuel gas is preheated to 1073 K before entering the cell. The cathode side is open to air. The current collectors at the anode side are attached to the outer surfaces of both ends of the anode tube and the current collector at the cathode side is connected to the whole cathodic surface. The Ag wire with a silver mesh is used for current collection. The performance of the micro-tubular cell is measured after the open circuit voltage (OCV) of the cell reached 1.0 V.

Table 1
Input parameters to model [2,11,12].

Descriptions	Symbol	Value
Furnace interior diameter (mm)		6
Tubular interior diameter (mm)		1.47
Anode thickness (mm)		0.8
Cathode thickness (μm)		50
Electrolyte thickness (μm)		10
Anode length (mm)		49.6
Cathode length (mm)		5.1
Electrolyte length (mm)		26.1
Anode conductivity (S m^{-1})	σ_a	$95 \times 10^6 T^{-1}$ exp(−1150/T)
Cathode conductivity (S m^{-1})	σ_c	$42 \times 10^6 T^{-1}$ exp(−1200/T)
Electrolyte conductivity (S m^{-1})	σ_{ele}	3.34×10^4 exp(−10300/T)
Anode thermal conductivity (W m^{-1} K^{-1})	k_a	1.86
Electrolyte thermal conductivity (W m^{-1} K^{-1})	k_{ele}	2.16
Cathode thermal conductivity (W m^{-1} K^{-1})	k_c	5.84
Anode density (kg m^{-3})	ρ_a	3310
Electrolyte density (kg m^{-3})	ρ_{ele}	5160
Cathode density (kg m^{-3})	ρ_c	3030
Anode specific heat capacity (J kg^{-1} K^{-1})	$C_{P,a}$	450
Electrolyte specific heat capacity (J kg^{-1} K^{-1})	$C_{P,ele}$	430
Cathode specific heat capacity (J kg^{-1} K^{-1})	$C_{P,c}$	470
Transfer coefficient	β	0.5
Electron transferred per reacting	n_e	1
Permeability (m^2)	K	1×10^{-12}
Molar entropy change of cathode reaction (J mol^{-1} K^{-1})	ΔS_c	81.63
Thermal radiative emissivity	ε_{rad}	0.3

3. Numerical model

The model makes use of the differential equations which are integrated in the 2D domains, through a commercial software, COMSOL MULTIPHYSICS®. Fig. 2 depicts the 2D schematic of the cell used for the numerical simulation. The input parameters of the model are shown in Table 1. The outputs of the model are the distributions of temperature, current density and thermal stress.

3.1. Model assumptions

- The model is based on steady state, using humidified H_2 as the fuel.
- Gas flow in the electrode channel is a fully developed laminar flow.
- The reactant gas mixtures are approximated as ideal gas and incompressible. The fuel cell operates with 100% current efficiency.
- The electrochemical reactions are considered to only take place at the electrode/electrolyte interface.
- The effect of gas on thermal conductivities of porous electrodes is neglected.

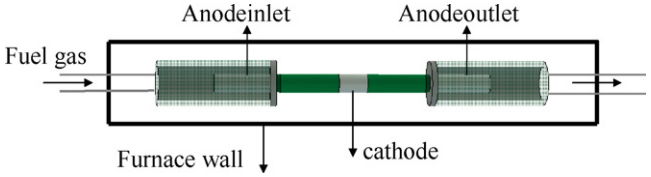

Fig. 1. The diagram of the micro-tubular cell reactor.

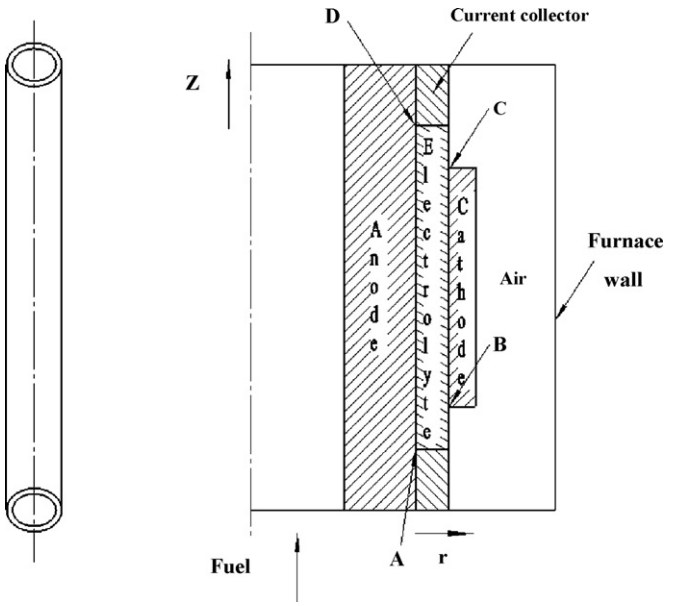

Fig. 2. Schematic of a micro-tubular geometry in the axisymmetric 2D model.

3.2. Electrochemical model

The Butler–Volmer kinetic equations are generally adopted for expressing the local current density distribution.

$$i_a = i_{a,0}^{H_2} \cdot (p_{H_2})^{0.25} (p_{H_2O})^{0.5} \left\{ \exp\left(\beta \frac{n_e \cdot F \cdot (\phi_{rev} - |\phi_a - \phi_{ele}|)}{R_g \cdot T} \right) - \exp\left[-(1-\beta) \frac{n_e \cdot F \cdot (\phi_{rev} - |\phi_a - \phi_{ele}|)}{R_g \cdot T} \right] \right\} \quad (1)$$

$$i_c = i_{c,0}^{O_2} \cdot \frac{(p_{O_2}/p_{O_2}^0)^{1/4}}{1 + (p_{O_2}/p_{O_2}^0)^{1/2}} \left\{ \exp\left(\beta \frac{n_e \cdot F \cdot (\phi_{rev} - |\phi_c - \phi_{ele}|)}{R_g \cdot T} \right) - \exp\left[-(1-\beta) \frac{n_e \cdot F \cdot (\phi_{rev} - |\phi_c - \phi_{ele}|)}{R_g \cdot T} \right] \right\} \quad (2a)$$

$$p_{O_2}^0 (\text{Pa}) = 4.9 \times 10^3 \ \exp\left(-\frac{2 \times 10^5}{R \cdot T} \right) \quad (2b)$$

In Eq. (1) it is adopted that the reaction order is 0.25 for H_2 and 0.5 for H_2O [8]. The cathodic exchange current density can be formulated from the Ref. [7], where $p_{O_2}^0$ can be found. Since some of the parameters could not be obtained directly from experiments or published literature, fitting processes have to be involved in this study. In Eqs. (1) and (2a), $i_{a,0}^{H_2}$ and $i_{c,0}^{O_2}$ are the adjustable parameters to fit the experimental data. $i_{a,0}^{H_2}$ is 7500 A m^{-2} for the anode and $i_{c,0}^{O_2}$ is 2200 A m^{-2} for the cathode. ϕ_{rev} can be obtained from Nernst equation. Electron and ion charge conservation at the electrode and electrolyte is expressed by Eq. (3).

$$-\nabla(\sigma \cdot \nabla\phi) = 0 \quad (3)$$

3.3. Thermo-fluid equations

The steady-state incompressible Navier–Stokes equation, Eq. (4) is solved to calculate the velocity distribution in the gas channel, and the Brinkman equation, Eq. (5) is used for the porous electrode.

$$\rho(u \cdot \nabla u) - \mu(\nabla^2 u) + \nabla P = 0 \quad (4)$$

$$\nabla P = \mu \cdot \nabla^2 u + \left(\frac{\mu}{K} \right) \cdot u \quad (5)$$

The steady state diffusion and convection equation, Eq. (6) is solved to obtain the species distribution in all domains.

$$\nabla(-D_{ij} \cdot \nabla c_i + c_i \cdot u) = 0 \quad (6)$$

In this model, the conductive and convective equation, Eq. (7) is used to calculate the temperature distribution in all subdomains:

$$\nabla(-k \cdot \nabla T) + \rho \cdot C_P \cdot u \cdot \nabla T = Q \quad (7)$$

Eq. (8) is used to express the radiative heat transfer between the outer surface of the cell and the furnace wall.

$$q_{rad} = \sigma_0 \cdot \varepsilon_{rad} (T^4 - T_{wall}^4) \quad (8)$$

The ohmic heating at the electrode and electrolyte is calculated by Eq. (9).

$$Q = \sigma \cdot \nabla^2 \phi \quad (9)$$

The heat of the electrochemical reactions entropy change is estimated by Eq. (10).

$$q_{rev,electrode} = \frac{T \cdot \Delta S_{electrode} \cdot i_{electrode}}{2F} \quad (10)$$

The $\Delta S_{electrode}$ denotes the molar entropy change of the electrode reaction at the local reacting temperature and pressure [11]. The heat of the ion transfer across the electrode/electrolyte interfaces is calculated by Eq. (11), where η_{act} can be found from Eq. (12).

$$q_{irr,electrode} = \eta_{act,electrode} \cdot i_{electrode} \quad (11)$$

$$\eta_{act} = \phi_{rev} - |\phi_{electrode} - \phi_{ele}| \quad (12)$$

3.4. Structural mechanics model

Thermal stresses in the three-layered structure (anode, electrolyte and cathode) are calculated using the structural mechanics module of the commercial finite element software COMSOL. The temperature field can be imported into the structural mechanics module and the stress field can be solved. In Table 2, the Young's modulus, the thermal expansion coefficient and the Poisson's ratio of the cell materials used in the study are given, which are assumed to be constant over a range of 273–1723 K. All materials are assumed to be isotropic.

The value of the zero stress temperature is very important for the determination of the magnitude of the stress. Many uncertainties remain in this area. A thin film of the YSZ electrolyte is deposited on the anode tube at a temperature of 1723 K. At this temperature both the anode and the electrolyte film are stress-free in the present work. A LSM/YSZ composite cathode is fired on the YSZ film at 1523 K. At this temperature the cathode is stress-free.

In this model when hydrogen is introduced and NiO is reduced into Ni, no shrinkage is considered. That has currently been reported in open literatures during NiO/YSZ reduction [10,18]. The CTEs of NiO/YSZ and Ni/YSZ are considered to be equal in this paper. This was also considered in open literature [10]. When the above-mentioned two assumptions are adopted in this model, it is acceptable to only calculate the stress distribution for the Ni/YSZ anode in the model.

Finally, the thermal stress equation is solved at the cell operating temperature. The fixing of the tubular SOFC is modeled by constraining the axial displacement at the fuel inlet boundary. The

Table 2
Material properties of the cell components.

	Young's modulus (GPa)	Poisson's coefficient	Coefficient of thermal expansion (K^{-1})	Characteristic strength (MPa)	Weibull modulus	Reference volume (mm^3)
Cathode	35 [6]	0.25 [6]	11.7×10^{-6} [16]	52 [10]	4 [10]	2.81 [10]
Electrolyte	183 [17]	0.32 [15]	10.8×10^{-6} [16]	282 [10]	8 [10]	0.27 [10]
Anode	57 [17]	0.17 [15]	12.2×10^{-6} [16]	115.2 [17]	6 [6]	0.578 [10]

other boundaries are free and the analysis is fully elastic. Thermal loads are introduced into the model according to the following equations, Eqs. (13) and (14).

$$\varepsilon_{th} = \alpha \cdot (T - T_{\text{ref}}) \tag{13}$$

$$\sigma_s = D \cdot (\varepsilon_t - \varepsilon_{th}) \tag{14}$$

According to the generalized Hook's law, the following elasticity matrix D, Eq. (15) is used for an isotropic material at the 2D axisymmetrical model.

$$D = \frac{E}{(1+\nu)(1-2\nu)} \begin{bmatrix} 1-\nu & \nu & \nu & 0 \\ \nu & 1-\nu & \nu & 0 \\ \nu & \nu & 1-\nu & 0 \\ 0 & 0 & 0 & \frac{1-2\nu}{2} \end{bmatrix} \tag{15}$$

3.5. Failure probability calculation

The rupture often occurs at the MEA due to the brittle nature of the ceramic. For this reason, it is valuable to analyze the failure probability of the MEA. The Weibull approach is considered to estimate the risk of rupture of the MEA in this model. The Weibull analysis [6] calculates the failure probability (P_f) of the MEA with the tensile stress:

$$P_{f,j} = 1 - \prod_{i=1}^{3} \exp\left(- \int_V (\sigma_i/\sigma_{s,0})^m dV_j/V_{j,0} \right) \tag{16}$$

where $\sigma_{s,0}$, m and V_0 represent the characteristic strength, the Weibull modulus and the reference volume, respectively. The different materials have a different Weibull modulus, which can be obtained experimentally. A greater Weibull modulus indicates that the material has higher reliability. The Weibull modulus of the anode used in this study was adopted of Ref. [6]. The subscript i (1, 2, and 3) denotes three principal stresses, σ_1, σ_2 and σ_3. The subscript j denotes the cell components, including anode, electrolyte and cathode. The input Weibull parameters for SOFC materials used in this model are listed in Table 2.

4. Results and discussion

4.1. Model validation

The cell performances obtained from the model are compared with the experimental performance data as shown in Fig. 3. The simulation results show that the calculated polarization curves agree very well with the experimental data. This demonstrates that the present model is accurate enough for studying the behavior of a tubular SOFC operating with humidified hydrogen.

4.2. Current density distribution in the anode

To understand the current flow in the anode, this paper gains three current densities at the different dimensions which are parallel to z direction and are evenly distributed in the anode. Their distances to the central symmetrical axis are 0.935 mm, 1.135 mm, 1.335 mm, respectively. To compare the current flow at the different anodic locations, the model calculates the r and z direction component of current density along fuel flow direction at the

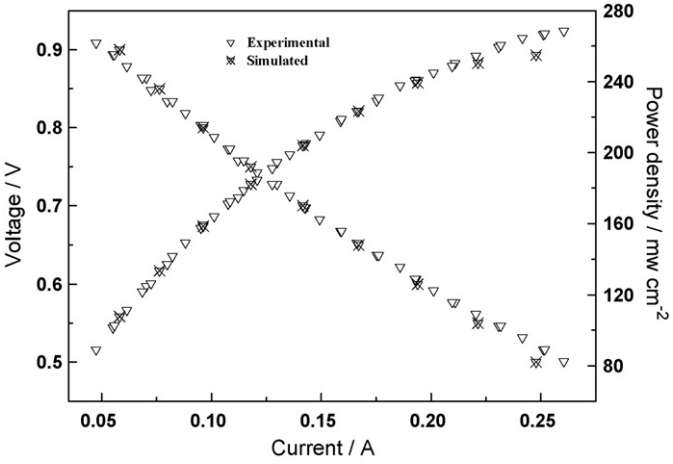

Fig. 3. Comparison of simulated and experimental performance data.

above-mentioned three r dimensions. Fig. 4 shows the r direction component of current density along fuel flow direction at the different r dimension (r = 0.935 mm, 1.135 mm, 1.335 mm) at 0.7 V. From Fig. 4, it is found that the r direction components of current density close to current collectors are a large negative value at all three dimensions. The above phenomena show that the current mainly flows from the outer surface nearby the current collectors to the anode inside, and the flowing direction points to the central symmetrical axis. The absolute value of current density gradually decreases from 1.335 mm to 0.935 mm. These results indicate that the r direction components of the current density close to the current collectors are bigger than those at other positions. After the current flows into the anode, the r direction components of current density all become zero. When the current reaches the anodic reactive zone at the middle of cell, the current value becomes positive. The phenomena show that the r direction components of the current density flow into the electrolyte.

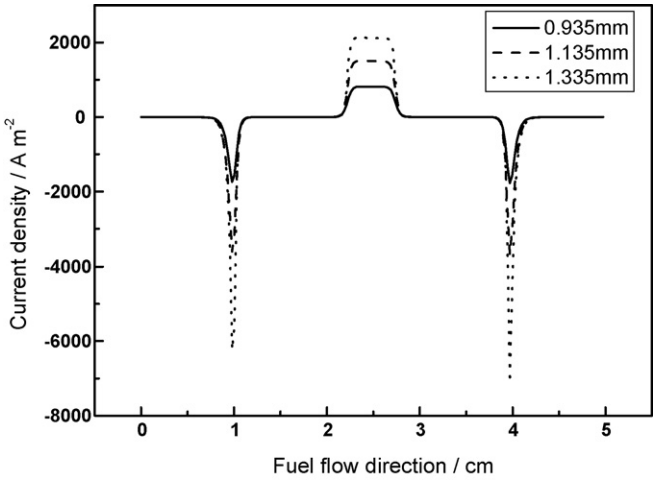

Fig. 4. The r direction component of current density along fuel flow direction at the different r dimension (r = 0.935 mm, 1.135 mm, 1.335 mm) at 0.7 V.

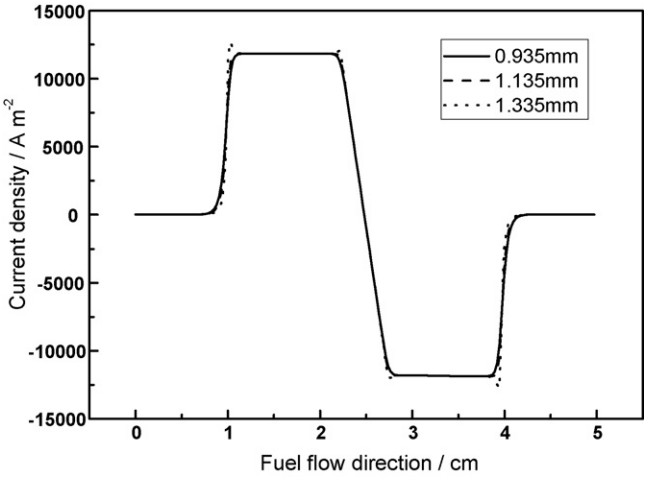

Fig. 5. The z direction component of current density along fuel flow direction at the different r dimension (r = 0.935 mm, 1.135 mm, 1.335 mm) at 0.7 V.

Fig. 5 shows the z direction component of current density along fuel flow direction at the different r dimension (r = 0.935 mm, 1.135 mm, 1.335 mm) at 0.7 V. From Fig. 5, it is found that the z direction components of current density begin to appear close to the current collectors at all three different dimensions. Because the current flow direction at fuel outlet is opposite to that at fuel inlet, the current density value at outlet is negative. After the current flows into the anode, the z direction current components at both ends rapidly increase and the absolute values at all three different dimensions are almost equal. From Figs. 4 and 5, in the process of transferring current to the reactive zone of the cell, the r direction components of current density are zero and the absolute values of z direction current density are the same. It indicates that the current transport is even at every investigated position. When the current reaches the reactive zone of the cell, the absolute values of the z direction current sharply decrease. Compared with Fig. 4, it can be seen that the decrease is because the z direction current components are transferred to the r direction current components and then flow into the electrolyte.

4.3. Temperature distribution in the cell

Fig. 6 shows the temperature change curve along anode outer surface including anode/electrolyte interface under the different load conditions. From Fig. 6, it is shown that when the cell voltage

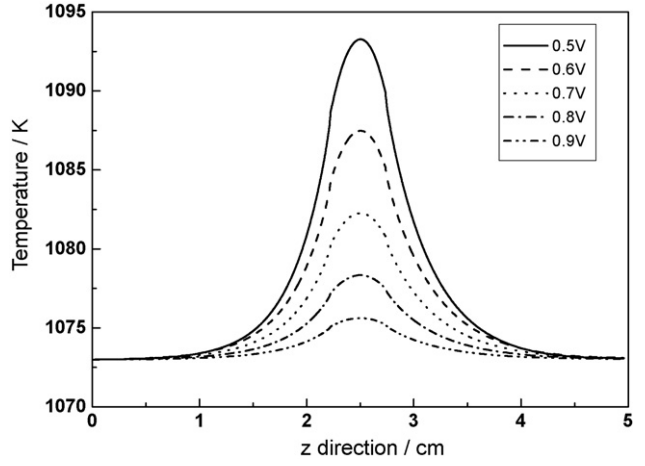

Fig. 6. The temperature change curve along the anodic outer surface including the anode/electrolyte interface at the different load condition.

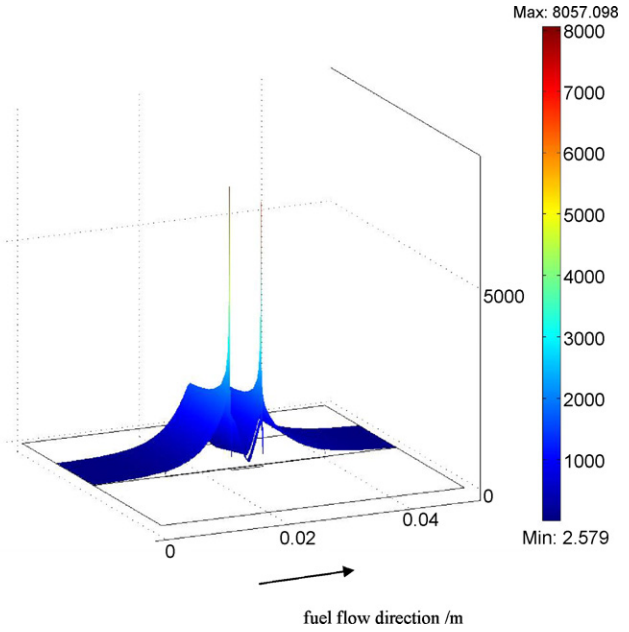

Fig. 7. Temperature gradients distributions (K m^{-1}) at 0.7 V.

decreases from 0.9 V to 0.5 V, the temperatures at the reactive zone of the cell gradually increase and the temperature maximum is at the cell center along z direction. The maximum reaches 1093 K at 0.5 V. This result indicates that although the cell locates at a constant temperature furnace, because plentiful heat is released at the electrochemical reaction, the cell temperature is always higher than the furnace temperature at the cell operating condition. The cell temperature rapidly decreases at the inert zone of the cell.

Fig. 7 shows temperature gradients distributions in the cell at 0.7 V. From Fig. 7, it is shown that firstly, the temperature gradient gradually increases from both ends of anode to the cell center, and the maximum temperature gradient is at the double ends (points B and C) of the reactive zone of the cell, and that secondly the temperature gradient gradually decreases from the double ends of the reactive zone of the cell to the middle of the cell. From Figs. 6 and 7, it is found that the temperature gradient at the position of the temperature maximum is smaller than at other positions of the reactive zone of the cell.

4.4. Thermal stress analysis

Fig. 8 shows the arrow plot of the principal stress at 0.7 V. The arrows express the principal stress directions, and the arrow sizes are proportional to the principal stress value. The part enclosed by the circle in Fig. 8(a) is scaled up to Fig. 8(b) and the part enclosed by the circle in Fig. 8(b) is scaled up to Fig. 8(c). The inward arrow expresses the compressive stress; the outward represents the tensile stress. In Fig. 8, it is shown that the principal stress is much larger in the electrolyte than in other parts. The principal stress in the electrolyte is mainly compressive along the z-axis.

The cell presents some material and geometrical singularities at its edges A, B, C, and D in Fig. 2 according to the Refs. [10] and [14]. Because of the high stress level close to the above-mentioned edges, these positions in the cell are potentially harmful for the cell structure. Fig. 9 shows the first principal stress distribution at 0.7 V. In strength theory, principal stress is stress in the principal plane which is free of shear stress. There are three principal stresses, σ_1, σ_2 and σ_3. By comparing the value, the order is determined, $\sigma_1 > \sigma_2 > \sigma_3$. In Fig. 9, the stress in the anode is tensile below 7 MPa except at the cell singular points. The stresses in the cathode and

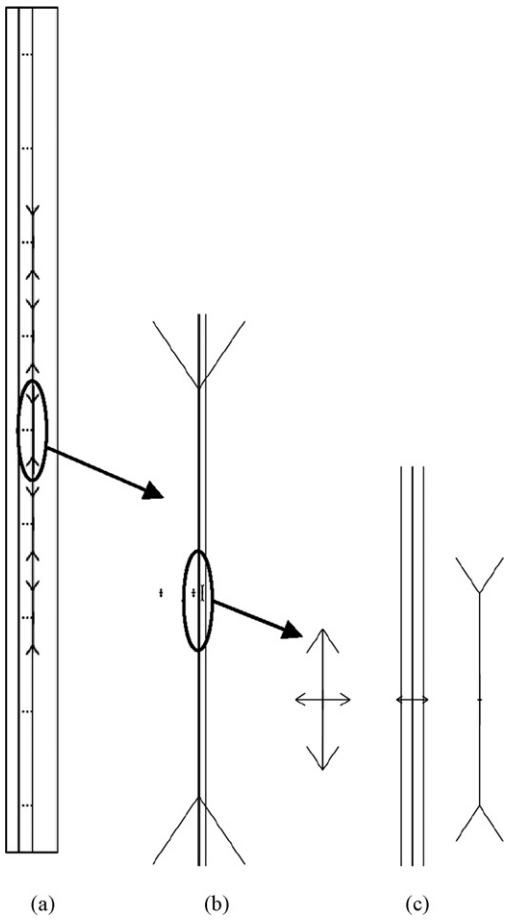

Fig. 8. The arrow plot of the principal stress at 0.7 V. The part enclosed by the circle (a) is scaled up to (b), and then the part enclosed by the circle in (b) is scaled up to (c).

electrolyte are compressive, primarily due to the lower CTE of the cathode and the electrolyte materials. The maximum of the first principal stress locates close to the both ends of the electrolyte, points A and D, due to material and geometrical singularities. From the Ref. [10], the cell singularities are harmless under the proper

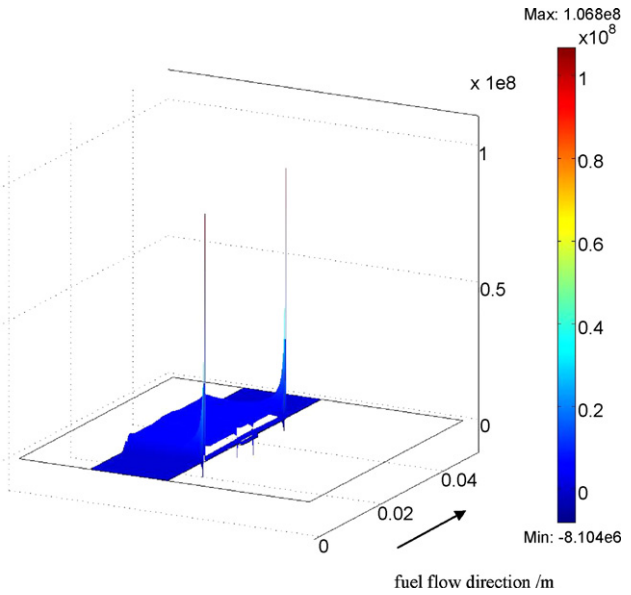

Fig. 9. The first principal stress distribution (Pa) at 0.7 V.

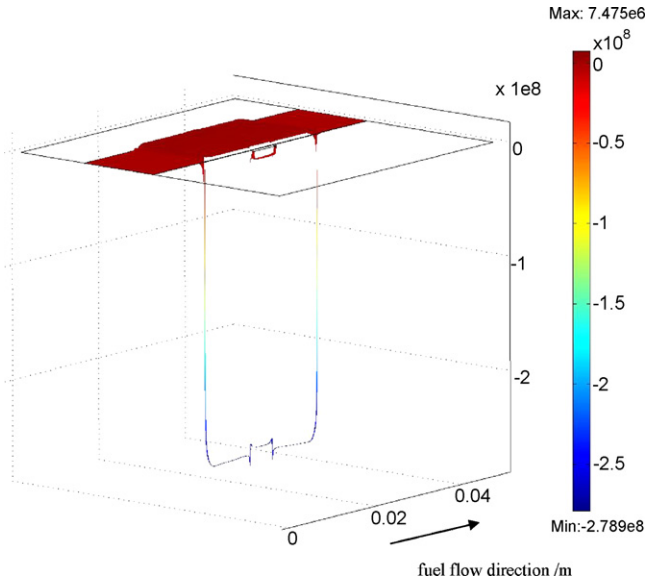

Fig. 10. The second principal stress distribution (Pa) at 0.7 V.

cell edge structure, so the singularities' effect on the cell failure is not considered in this paper.

Figs. 10 and 11 show the second and third principal stress at 0.7 V. In Figs. 10 and 11, it is shown that the stress is strongly compressive about 270 MPa in the whole electrolyte. The compressive stress in the cathode is less than 10 MPa. It is known that compared with compressive stress, tensile stress is easier to cause ceramic material fracture. The above results indicate that the cathode is relatively stable under a low level of compressive stress. The compressive stress in the electrolyte is much higher, but still below the failure level because the fracture strength of electrolyte at the compressive condition has been reported to be about 1 GPa [13].

4.5. Failure probability analysis

The specific values of the stress field cannot provide a failure probability at any particular operating point. In order to investigate the effects of the stress on the MEA reliability, the Weibull approach

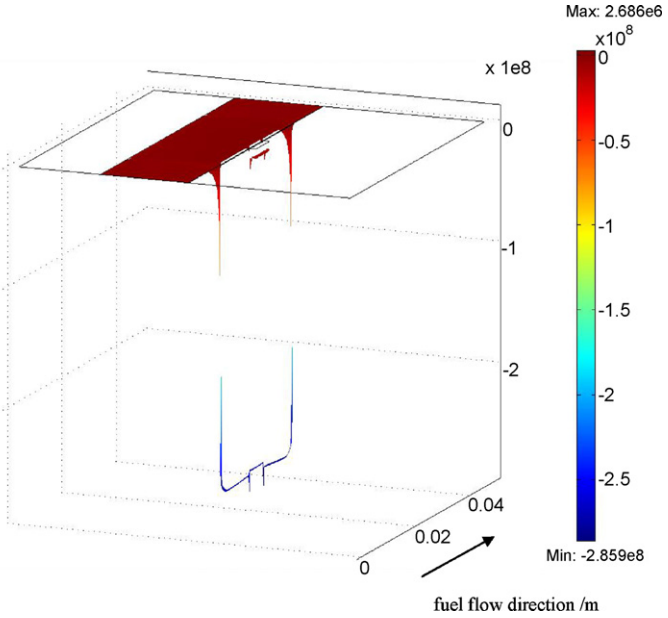

Fig. 11. The third principal stress distribution (Pa) at 0.7 V.

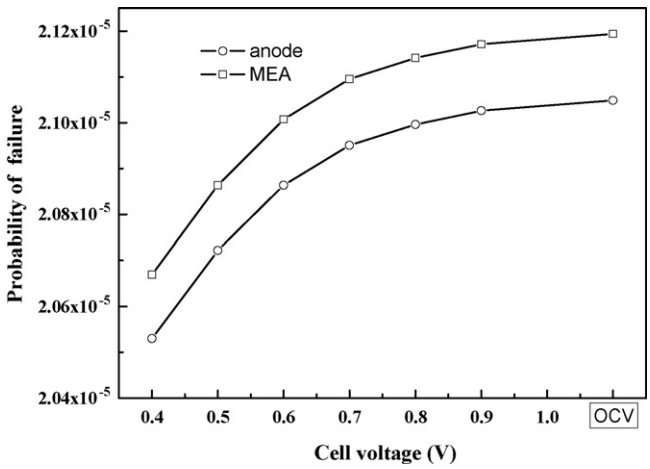

Fig. 12. Failure probability of the anode and MEA with various voltage of the cell.

is developed, and by which the influences of the cell voltage on failure probability are researched. The influences of the cell voltage on the failure probabilities of the anode, MEA, cathode and electrolyte are shown in Figs. 12 and 13, respectively. The results indicate that failure probabilities of the all parts except the cathode increase with the increase of the cell voltage. The probability of failure is lower at low load in the cell components because the effect of the temperature is stronger than that of the temperature gradient in the cell. In the cathode, on the other hand, the probability of failure is lower at high load when the effect of thermal gradients is stronger than that of the temperature. However, it has to be mentioned that the results in this model are limited to a particular choice of material properties.

Weibull analysis only calculates a positive value. With regard to the calculation of the stress field, the tensile stress is positive and the compressive is negative. The stress in the anode is mostly tensile; the stresses in the cathode and the electrolyte are mostly compressive. So, the results of the probability of a failure of the cathode and the electrolyte are much smaller than that of the anode. From Fig. 12, it is found that the failure probabilities of the anode and MEA are at the same order of magnitude. So, it can be considered that the failure probability of the anode is the decisive factor of the failure probability of the MEA. As shown in Figs. 12 and 13, the difference of the failure probabilities between the cell operating state and the open circuit is less than 3%. From Figs. 7 and 9, it can be also found that when the maximum temperature gradient has attained 8000 K m^{-1}, the anodic tensile stress is still below 7 MPa. These phenomena indicate that the micro-tubular cell can resist the high

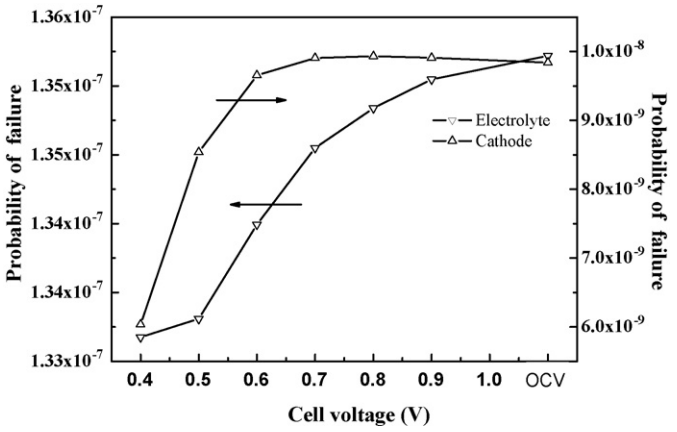

Fig. 13. Failure probability of the electrolyte and cathode with various voltage of the cell.

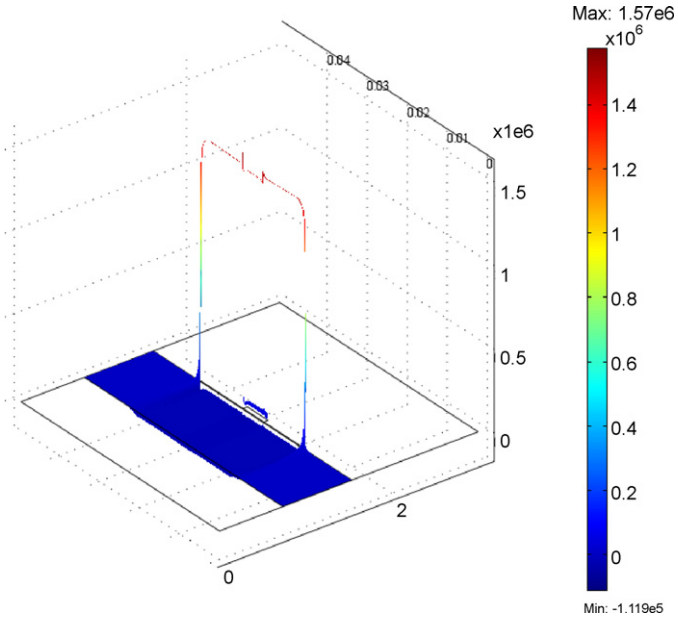

Fig. 14. The cell strain energy density (J m^{-3}) at 0.7 V.

thermal shock and that the cause of stress is mainly the residual stress due to the mismatch between the CTE of the materials of MEA.

The residual stress is caused by the different CTEs of the electrolyte membrane and electrodes. When the CTEs of all components are the same and the temperature is constant, no stress can be found in the cell. In the anode-supported SOFC, the CTE difference between the anode and electrolyte membrane is the decisive factor of the stress in the cell. Compared with the electrolyte, the CTE of the anode is easy to adjust. Because the CTE of the anode is higher than that of the electrolyte, an effective method to decease the failure of probability of the cell is to decrease the CTE of anode.

Though the above analysis has proved that the tubular cell can operate safely enough, the Weibull approach is only applied at tensile stress condition. Failure at interfaces between electrolyte film and anode substrate will happen if the film is subjected to a sufficient high compressive stress so that the elastic strain energy stored in the film exceeds the energy required. Actually, the high compressive stress can cause the layer to fail when an interfacial defect occurs or a critical tensile stress is applied on the layer. In this work, the risk of failure has been investigated by calculating the elastic strain energy stored in the compressive thin layer. Fig. 14 shows the cell strain energy density at 0.7 V. The strain energy stored in the cathode layer is only about 44 kJ m^{-3}, whereas the energy stored in the electrolyte layer reaches 1575 kJ m^{-3}. This value exceeds the energy requirement of the electrolyte film (ca. 1000 kJ m^{-3} [10]). So, the failure can arise if there is an interfacial flaw or a high enough tensile stress applied at the electrolyte.

Several limitations of this simulation method exist. Such as, in the SOFC, the electrodes are porous. If a micro-scale electrode can be added in this macroscopic model and a multiscale model is used, the model can show more information and more accuracy about the stress distribution. At the process of the anodic reduction, several assumptions are considered in this model. After the reduction, the micro-morphology of anode is very important for the cell performance. The micro-morphology change from NiO/YSZ to Ni/YSZ can be taken into account in detail in the future.

5. Conclusions

A 2D SOFC model is constructed in this study to evaluate the thermal-fluid behavior, electrochemical reaction and thermal stress

in a SOFC single cell. The temperature distribution is the inputs for a finite element software, which is used to estimate the thermal stress field. The experimental data are employed to validate the simulation results. Good agreements have been observed between simulation results and experimental data. The current flow phenomena in the anode are analyzed in detail. The result indicates that the current transport in the anode is the same at every investigated position. The temperature gradient at the position of the temperature maximum is smaller than at other positions of the reactive zone of the cell. The micro-tubular SOFC can resist the high thermal shock and the stress occurs mainly because of the residual stress due to the mismatch between the CTE of the materials of MEA. It is not recommended to keep a quite slow rate of sintering temperature at the process of the SOFC manufacture, especially at high temperature because the stress is smaller close to the stress-free temperature. The effective method to decease the failure of probability of the cell is to decrease the CTE of anode for anode supported SOFC. Matching the CTEs is the most important factor to attain a higher reliability of the cell. Through the Weibull analysis it has been proved that the tubular cell can operate safely, the cell failure can arise if there is an interfacial flaw or a high enough tensile stress applied at the electrolyte. In the process of SOFC operation, one should pay attention to impose the external force as low as possible.

Acknowledgments

The authors gratefully acknowledge financial supports from the Ministry of Science and Technology of China (Nos. 2004CB719506, 2005CB221404 and 2006AA05Z147) and Natural Science Foundation of China (Nos. 20676132 and 20876156).

References

[1] S.C. Singhal, K. Kendall, High Temperature Solid Oxide Fuel Cells: Fundamentals, Design and Applications, Kidlington Oxford, Elsevier, 2003.
[2] D.A. Cui, L. Liu, Y.L. Dong, M.J. Cheng, J. Power Sources 174 (2007) 246–254.
[3] A. Selimovic, M. Kemm, T. Torisson, M. Assadi, J. Power Sources 145 (2005) 463–469.
[4] D.A. Cui, M.J. Cheng, AIChE J. 55 (2009) 771–782.
[5] D. Sanchez, R. Chacartegui, A. Munoz, T. Sanchez, J. Power Sources 160 (2006) 1074–1087.
[6] A. Nakajo, C. Stiller, G. Harkegard, O. Bolland, J. Power Sources 158 (2006) 287–294.
[7] H. Zhu, R.J. Kee, V.M. Janardhanan, O. Deutschmann, D.G. Goodwin, J. Electrochem. Soc. 152 (2005) A2427.
[8] W.G. Bessler, S. Gewies, M. Vogler, Electrochim. Acta 53 (2007) 1782–1800.
[9] W. Fischer, J. Malzbender, G. Blass, R.W. Steinbrech, J. Power Sources 150 (2005) 73–77.
[10] J. Laurencin, G. Delette, F. Lefebvre-Joud, M. Dupeuxb, J. Eur. Ceram. Soc. 28 (2008) 1857–1869.
[11] K. Kanamura, S. Yoshioka, Z. Takehara, J. Electrochem. Soc. 138 (1991) 2165–2167.
[12] B. Todd, J.B. Young, J. Power Sources 110 (2002) 186–200.
[13] T. Kato, N.S. Wang, A. Negishi, A. Momma, Y. Kasuga, A. Nozaki, Proceedings of the Third International Fuel Cell Conference, Nagoya, Japan, 1999, p. 461.
[14] D. Leguillon, E. Sanchez-Palencia, Computation of Singular Solutions in Elliptic Problems and Elasticity, J. Wiley and Masson, New York, Paris, 1987.
[15] A. Atkinson, A. Selcuk, Solid State Ionics 134 (2000) 59–66.
[16] N.Q. Minh, T. Takahashi, Science and Technology of Ceramic Fuel Cells, Elsevier, 1995.
[17] M. Radovic, E. Lara-Curzio, Acta Mater. 52 (2004) 5747–5756.
[18] T. Klemenso, C. Chung, P.H. Larsen, M. Mogensen, J. Electrochem. Soc. 152 (2005) A2186–A2192.